

Understanding the Conductance Dispersion of Single-Molecule Junctions

Zhi Li, Leopoldo Mejía, Jonathan Marrs, Hyunhak Jeong, Joshua Hihath,* and Ignacio Franco*

Cite This: *J. Phys. Chem. C* 2021, 125, 3406–3414

Read Online

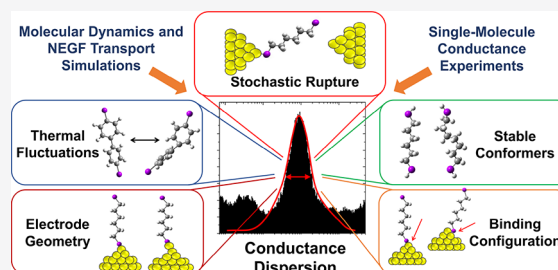
ACCESS |

Metrics & More

Article Recommendations

Supporting Information

ABSTRACT: Molecular junctions have emerged as a powerful tool to investigate chemistry and physics at the single-molecule limit. However, their utility as a platform to develop spectroscopies and construct molecular devices is limited by the broad conductance dispersion typically encountered in experiments. The current view is that such broad dispersion arises because the detailed junction configuration is uncontrollable and varies in and between experiments. Contrary to conventional wisdom, through atomistic simulations and experiments, we show that even in ideal conditions, where the electrodes and electrode-molecule binding configurations are perfectly well-defined, measurements will still exhibit a broad conductance histogram. Such dispersion arises because of conductance changes as the junction is mechanically manipulated and the unavoidable stochastic nature of junction rupture. The results offer detailed atomistic insights into the factors that contribute to the broad conductance histograms and identify the key physical aspects that need to be controlled to narrow its width.



1. INTRODUCTION

Creating precise atomic-scale electronic devices has been one of the ultimate goals of nanoscience and nanotechnology over the past several decades, and substantial progress has been made in the pursuit of these smallest-scale electronic systems through the advent and advancement of molecular-scale electronics.^{1–10} In addition to device applications, molecular electronics experiments have also emerged as a powerful and versatile platform where voltages, force, and light can be simultaneously applied^{11,12} and used to investigate chemistry and physics at the single-molecule limit.^{13–15}

However, despite this impressive progress as both a technology and a platform for interrogating basic molecular science, practically all single-molecule electronic systems exhibit a large dispersion of conductance values. This is thought to be due to the lack of control and uncertainty on the precise geometry of the junction.^{16–20} For this reason, the reproducibility in these experiments customarily relies on the acquisition of hundreds or thousands of single-molecule conductance traces in freshly formed molecular junctions using the break-junction (BJ) technique (or equivalents) to obtain statistically verifiable results.^{9,10} This results in highly reproducible conductance histograms but with a broad distribution of conductance values, typically with a standard deviation in the range of 1 order of magnitude (see Figure 1 center).

The broad conductance dispersion limits the applicability of molecular electronics as a platform for molecular spectroscopies and devices. From the spectroscopy perspective, while each experimental conductance trace measures the properties

of a single molecule, the inherent averaging that occurs when collecting data from hundreds of experimental realizations limits the utility of this class of measurements as a window into the single-molecule world. From a technological perspective, the broad distribution of conductances associated with a given molecular junction limits their use in applied electronics where reproducibility is an important feature. To overcome these problems and achieve better control over the junction properties, it is crucial to understand the factors that lead to the large dispersion of conductance values.

Existing experimental and theoretical efforts to understand the conductance histograms broadening have identified a variety of likely contributing factors.^{21,22} As schematically shown in Figure 1, possible contributing factors include inherent experimental uncertainties in electrode configuration^{23,24} and molecule-electrode binding,^{25,26} variations in the conductance due to the presence of different stable molecular conformers,^{27,28} gauche defect in alkanes,^{29,30} and thermal fluctuations in the lead,³¹ molecule,³² and molecule–leads contact.^{33,34} However, currently it is not understood which mechanism is dominant.

Received: September 15, 2020

Revised: December 14, 2020

Published: December 29, 2020



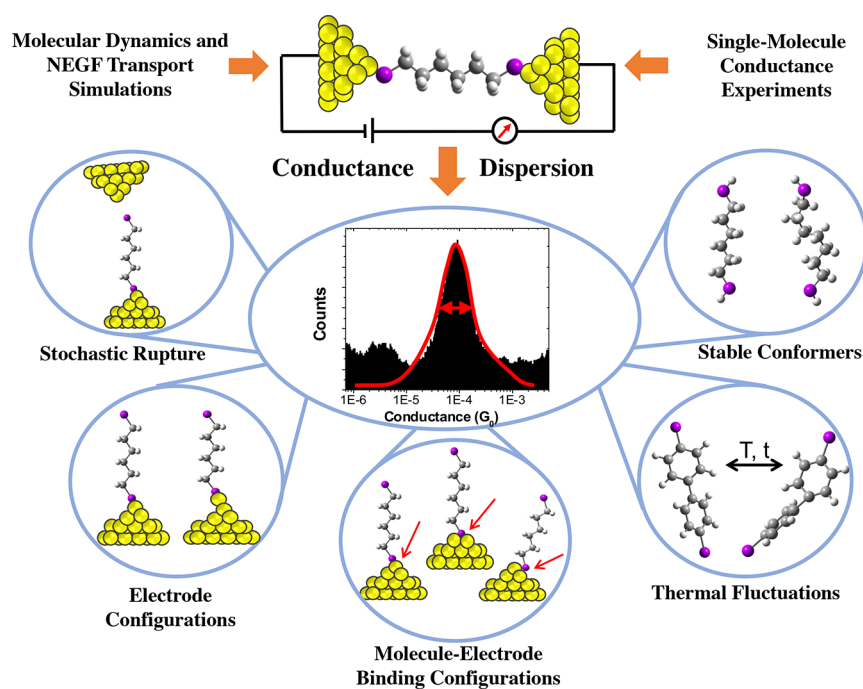


Figure 1. Possible contributing factors to the conductance dispersion in molecular electronics experiments. In experiments, thousands of single-molecule conductance measurements (top) must be performed in order to obtain a reproducible distribution of conductance values (center). This process results in a large dispersion of conductance that limits the applicability of molecular electronics in technology and spectroscopy. Through molecular dynamics simulations coupled to Green's function transport computations we examine different contributing factors to the dispersion of conductance histograms.

In ref 35, we discussed modeling aspects needed to connect theory with break junction experiments and simulate the conductance histograms. In this paper, through detailed atomistic simulations and experiments, we investigate possible contributing factors to the probability distribution $p(\log(G/G_0))$ of conductance G ($G_0 = 2e^2/h$ is the quantum of conductance) encountered in break junction experiments.

To explore how different molecular backbones and anchoring groups affect the conductance distributions, we considered a family of alkane–dithiols (alkane-DT, C_n DT) and alkane–methyl–sulfides (alkane–SMe, C_n SMe) with a varying number $n = 4–12$ of carbon atoms. We consider two cases: (i) The first is the distribution of conductances generated by all possible molecular snapshots encountered in a given experiment. This quantity is directly accessible to simulations and corresponds to hypothetical experiments with arbitrarily high time resolution. (ii) The second is the distribution of *time-averaged* conductances. This quantity reflects the conditions of usual experiments where currents are averaged over microseconds and do not resolve contributions by individual molecular snapshots.

The computational component of this work is based on classical atomistic molecular dynamics (MD) simulations of junction evolution and Landauer transport computations. We use them to examine the role of thermal fluctuations, electrode geometries, and molecule–electrode binding configurations on the conductance distributions. These computational observations are further tested with conventional and pull-and-hold STM-BJ experiments. The latter probe conductance without mechanically changing the electrode shape and can be used to determine the conductance histogram for a single junction monitored for a long time (up to seconds).

Surprisingly, we find that even under ideal conditions in which the initial electrode shape and binding configuration is identical between experimental realizations the time-averaged conductance traces will still exhibit a broad dispersion. Such dispersion arises due to changes in conductance during mechanical elongation and the stochastic nature of junction rupture, previously overlooked factors that play a key role in determining the conductance histograms.

The structure of this paper is as follows. Section 2 describes the computational strategy for modeling break junction experiments and the experimental approach to obtain conductance traces and histograms. Then, Section 3.1 describes how thermal fluctuations, electrode geometries, stable conformers, and binding configurations influence the conductance distribution encountered during the dynamics. Subsequently, Section 3.2 discusses factors that determine the experimental conductance histograms, which are obtained from *time-averaged* currents. Our main results are summarized in Section 4.

2. METHODS

Break-junction experiments proceed by bringing an atomically sharp tip electrode into contact with a second electrode in the presence of the molecules of interest in solution. Once contact is made between the two electrodes, as can be determined from the current, the tip is withdrawn until the current reaches the resolution of the current amplifier (e.g., zero). If no molecules are bound between the electrodes, this withdrawal process results in a smooth exponential decay in the current. However, if molecules bind between the two electrodes, then steps occur in the current vs distance trace. By repeating this process thousands of times it is possible to perform a statistical analysis of the results to determine the most probable

conductance of a single-molecule junction for a given molecular species.

2.1. Computational Methods. To computationally model such break junction experiments and develop an atomistic understanding of the contributing factors to the broad conductance histograms, we used a combination of classical MD simulations of the junction formation and evolution with steady-state electronic transport computations using Green's function methods.³⁶ The modeling strategy employed is identical with that in ref 35. Briefly, the dynamics was followed using classical MD in the *NVT* ensemble (300 K) using the Langevin thermostat. The system was described by a Au–S–C–H reactive force field (reaxFF)³⁷ that allows bond breaking and making events that are essential to understand molecular electronics break junction experiments. The quasistatic mechanical elongation was performed by pulling at a speed of $v = 6 \times 10^{-7}$ Å/fs.

At the beginning of the pulling, the molecules were placed between the electrodes with an angle with respect to the surface to ensure that a molecular junction is formed in the simulations. The simulations were performed using electrodes with well-defined shape and sets of crushed electrodes constructed by mechanically forcing them into contact and subsequently pulling as in experiments.

In the simulations, the conductance histograms were modeled by computing the zero-bias Landauer transport for snapshots encountered during the MD. Specifically, the zero-bias conductance $G = G_0 T(E_{\text{Fermi}})$ was determined by computing the transmission at the Fermi energy $T(E_{\text{Fermi}})$ using Green's functions³⁸ and an extended Hückel Hamiltonian as implemented in Husky.^{36,39,40} In the method, the Fermi level E_{Fermi} of gold is an adjustable parameter chosen to be around the extended Hückel Au 6s orbital level (−10.92 eV). The precise value was chosen such that the peak of the experimental and computational conductance histograms coincide. In practice, $E_{\text{Fermi}} \approx -11.6$ eV for alkane–DT, and −11.25 eV for alkane–SMe. The specific Fermi levels employed in the different simulations are shown in Table 1. Additionally, Figure S1 in the Supporting Information shows how the conductance histograms are affected by this parameter.

To construct histograms, it is desirable to only include conductance of mechanically stable molecular junctions. As a

Table 1. Fermi Energies (eV) Employed in the Simulations and the Conductance Histogram Peak Positions ($\log(G/G_0)$) for Alkane–Dithiols and Alkane–Methyl–Sulfides Junctions in Figure 3

molecules	E_{Fermi}	peak
C4SMe	−11.2	−2.8
C8SMe	−11.25	−4.4
C8SMe (crushed)	−11.25	−4.4
C12SMe	−11.2	−6.0
C6DT (top–top)	−11.7	−3.4
C6DT (top–bridge)	−11.6	−3.0
C8DT (top–top)	−11.6	−4.2
C8DT (top–bridge)	−11.6	−3.6
C8DT (crushed)	−11.6	−3.6
C10DT (top–top)	−11.5	−5.1
C10DT (top–bridge)	−11.4	−4.7

criterion, we supposed that junctions with $\log(G/G_0) < -10.0$ correspond to broken systems and are not taken into account.

2.2. Experimental Methods. Alkanedithiol (C6DT, C8DT, and C10DT) experimental solutions were prepared by creating 100 μL of 5 μM alkanedithiol solution in mesitylene. A clean gold-coated (99.998% purity, 130 nm) mica substrate, which was stored in an inert and dry vacuum environment, was annealed using a butane flame. A Teflon ring cell was clamped onto the gold-coated mica substrate, and the experimental solution was then deposited into the Teflon cell to cover the gold substrate with the solution. The substrate was then placed into the head of a scanning tunneling microscope (STM). A new and clean piece of gold wire was cut and placed into the tip holder of the STM head. The sample and STM were enclosed within an isolation chamber to dampen any vibrational or acoustic shocks that might disturb the experiment. A specially designed LabVIEW program was used to control and collect data from the STM. The conductance trace data was acquired using the LabVIEW program to interface with the STM. The voltage of the piezo transducer in the STM head was controlled to slowly move the gold tip into and out of contact with the Au substrate in the experimental solution. For short lifetimes (<20 ms) the traces were obtained from regular STM tapping (with a constant pulling rate ~ 40 nm/s). For long lifetimes, the gold tip in the STM was moved down until contact was made with the gold-coated mica substrate, and the gold tip was then pulled up until a molecular junction was formed, which was indicated by a feedback algorithm that was used to detect the appearance of a step within 1 standard deviation of the peak conductance value. The gold tip was then held stationary while the conductance measurements were continuously acquired by applying the voltage bias and measuring the current. This current was amplified with a 10 nA/V transimpedance amplifier. The conductance measurements were acquired until the molecular junction broke down, as made evident by a sudden decrease in the current toward very low current values characteristic of an open circuit. The resulting data was then processed in a LabVIEW program to generate the conductance histograms and conductance traces.

3. RESULTS AND DISCUSSION

3.1. Factors Influencing the Conductance Distribution. We first focus on the factors that determine the conductance distribution generated by all molecular conformations encountered in the junction setting. The distribution depends parametrically on junction elongation L , as each L defines a different molecular ensemble. We consider the conductance distribution obtained by collecting data in the range $\Delta L = L - L_0$

$$p(\log(G/G_0)) = \frac{1}{|\Delta L|} \int_L^{L_0} p_{L'}(\log(G/G_0)) dL' \quad (1)$$

where L_0 is the elongation at which the junction breaks, and $p_{L'}(\log(G/G_0))$ is the conductance distribution for fixed L' . Such distribution is useful in understanding the atomistic events that lead to conductance dispersion that are not resolved in time-averaged quantities.

3.1.1. Role of Electrode Geometry and Stable Conformers. To explore the impact of electrode geometry on the conductance distribution, we attached $C_n\text{SMe}$ ($n = 6, 8,$ and 10) to three combinations of gold electrode pairs—pyramid–pyramid (PP), pyramid–flat (PF), and flat–flat (FF)—as specified in Figure 2c. The atomically sharp pyramids are seven

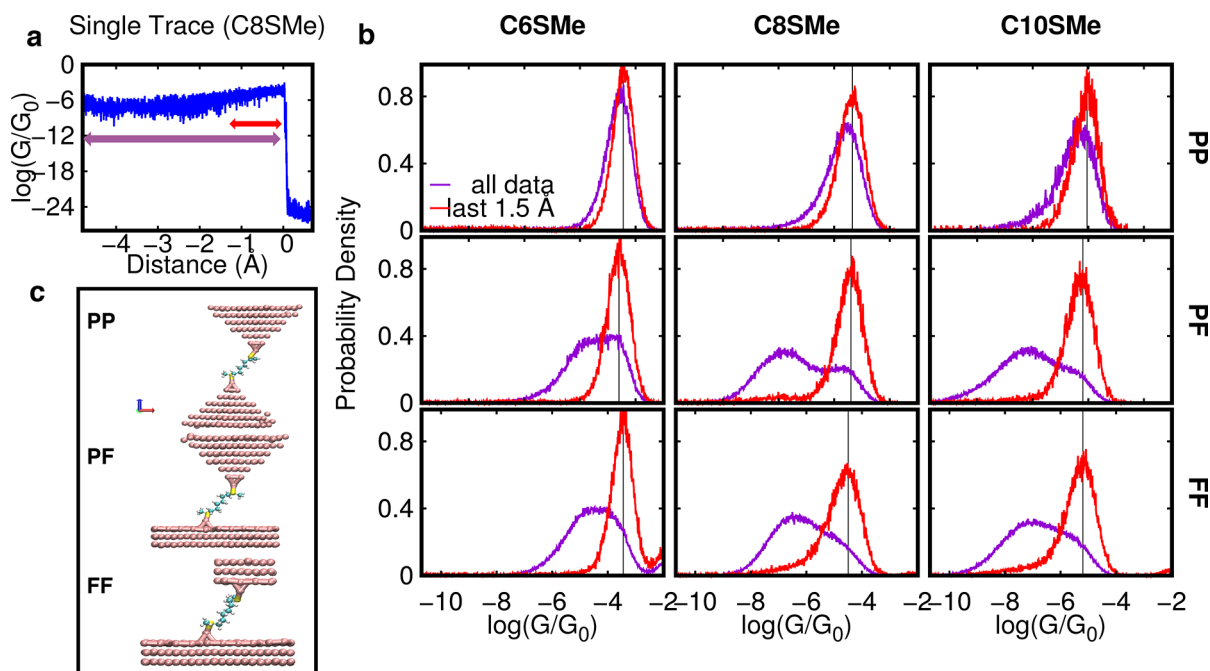


Figure 2. Dependence of simulated conductance histograms on the electrode geometry for alkane-methyl-sulfides ($C_n\text{SMe}$) with a varying number n of carbon atoms. (a) Typical conductance profile during the pulling of alkane-based molecular junctions (C8SMe attached to pyramidal electrodes). The conductance exhibits large scale thermal fluctuations and a characteristic conductance drop when the junction is mechanically broken. (b) Conductance probability density distributions for $C_n\text{SMe}$ connected to the types of electrodes pairs depicted in (c) pyramid–pyramid (PP), pyramid–flat (PF), and flat–flat (FF) moieties. Results summarize the statistics collected during 40 pulling trajectories. The panels contrast histograms constructed taking into account all data (purple lines) and only data collected in the last $\Delta L = 1.5 \text{ \AA}$ segment before breaking (red lines). Simulations were performed with a Fermi energy in the HOMO–LUMO gap and 0.38 eV below the extended Hückel Au $6s$ orbital energy. Note how the histograms constructed from extended junctions are essentially independent of the electrode geometries.

atoms deep while the Au(111) surfaces have three atomic layers and an extra apex atom to which the terminal S in the molecule is connected.

To illustrate the computational methodology, consider the conductance vs elongation trace shown in Figure 2a generated by a single MD trajectory for the C8SMe molecular junction initially in the PP geometry depicted in Figure 2c. At the beginning of pulling, due to compression of the molecule, the junction shows low conductance features near $10^{-6} G_0$. As the junction is mechanically extended, the conductance increases to $\sim 10^{-4} G_0$. In addition, the conductance exhibits thermal fluctuations in the $10^{-4} - 10^{-6} G_0$ range. The junction is pulled until it mechanically breaks as reflected by a sharp drop in the conductance.

To model the break junction process we generated 40 MD trajectories of junction evolution for each type of electrode pair, with identical initial configuration but different initial (random) velocities and set of random numbers in the Langevin evolution. Normalized histograms obtained from these traces are shown in Figure 2b. The plots include histograms constructed from all of the conductance values calculated throughout the pulling process (purple lines), and those constructed using only data collected during the last 1.5 \AA before junction rupture (red lines). When all available conductance data is employed, we observe that the distribution of conductance values critically depends on electrode shape. In this case, such a dependence reflects the fact that different electrode shapes lead to different ensembles of molecular conformations during pulling and to dispersion in the through-space molecule-electrode couplings.²⁹ Specifically, in comparison to the pyramidal electrodes, the nanoconfinement induced

by the flat electrodes (PF and FF in Figure 2b) leads to a higher proportion of alkanes with gauche conformations that have low conductance values. This is the origin of the bimodal distribution of conductance values observed for PF and FF electrode pairs.

By contrast, when only the last $\Delta L = 1.5 \text{ \AA}$ segment before breaking of the elongation process is taken into account, the histograms become largely independent of electrode shape. In fact, as shown in Figure 2b (red lines) for the three molecules considered, the shapes and widths of the histograms become essentially identical regardless of the electrode configuration. This is because the presence of gauche conformations and secondary through-space electrode-molecule couplings are suppressed by elongation, making the details of the electrode shape less important. As discussed in ref 35, decreasing the ΔL (within a range) does not influence the width of the main peak in the conductance histogram.

Therefore, in simulation where all instantaneous molecular snapshots are taken into account, the conductance distribution of elongated junctions are not sensitive to changes in the electrode geometry.

3.1.2. Role of Binding Configurations. To take into account possible effects due to molecule–electrode binding configurations, we contrast simulation results for alkane-based junctions with different bindings. We consider both thiol and methyl sulfide anchor groups. Methyl sulfides are known to exhibit a simple donor–acceptor binding to gold,^{41–43} while thiols can bind to apex gold atoms (top) or to sites between two gold atoms (bridge). The simulations are performed using a flat electrode and a pyramidal tip (PF in Figure 2c). For the thiol-terminated alkanes, in the computations we favored an

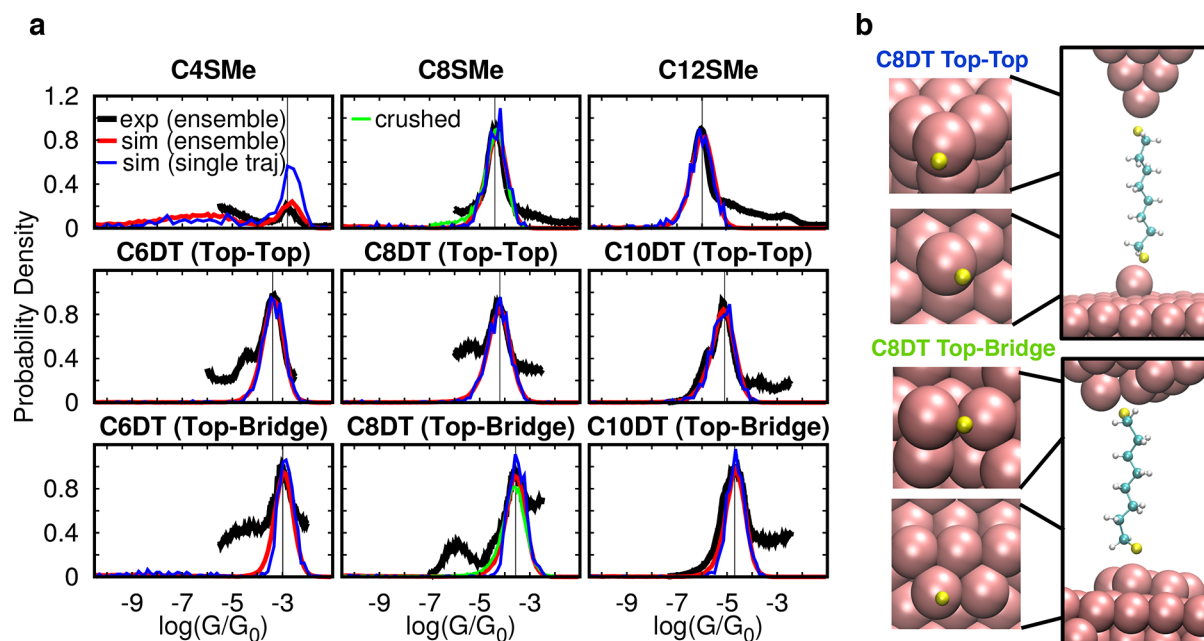


Figure 3. Simulated and experimental conductance histograms for alkane-based molecular junctions. The plot compares experimental (black) and simulated conductance distribution for a family of alkanes with methyl sulfide (top panel), and thiol anchor groups in top–top (middle panel) and top–bridge (bottom panel) binding configuration. In simulations, only data collected in the last piece ΔL before breaking are considered. The Fermi energy is chosen to be around the 6s Au orbital energy with its precise value selected such the position of the peak in the experimental and simulated distributions coincide (see Table 1). Simulations include distributions obtained from an ensemble average over 40 pulling trajectories using the same initial electrodes (in red), an ensemble of 60 precrushed electrodes (in green) with an uncontrolled distribution of electrode geometries, and results using just one MD trajectory (in blue). Note that binding configurations can cause the emergence of different conductance peaks. The broad conductance distributions arise due to thermal fluctuations and not due to uncertainties in the electrode configuration. Note that even when experimental curves apparently coincide with simulations, the comparison is not strict as experiments average over time. Experimental data for C4SMe–C12SMe were provided by Professor Latha Venkataraman.

initial type of binding configuration by positioning one thiol groups within bonding distance to an apex atom in the tip and the surface (top-top configuration, middle panel), or to an apex atom in the surface and to a truncated pyramidal tip (top–bridge configuration, lower panel).

It is well-known that changing the binding configurations changes the conductance for alkanedithiol.²⁶ To see this in our simulations, consider the conductance distribution of C8DT in both top–top and top–bridge binding configuration; see Figure 3a. In these two cases, we employed the same E_{Fermi} to match experiments. We find that the conductance histograms with top–bridge binding show higher conductance and are narrower (in log plots) than top–top binding. This shows that different binding configurations result in different sets of conductance values, whose most probable conductance and histograms' width are different. In general, depending on how different is the conductance between all the possible binding configurations and how stable is each of them, this leads to multiple peaks, shoulders or a merged broader conductance histogram.

To see the effect of the contribution of multiple binding configurations to the resulting histogram when no configuration is favored in the initial conditions, we performed simulations with an uncontrolled junction geometry and binding configuration for C8SMe and C8DT (Figure 3a, green lines). For this, we generated an ensemble of junctions with crushed electrode geometries as detailed in ref 35 and used it to generate the conductance histograms. In this case, no definitive preference for the binding configuration is enforced. Instead, at initial time each terminal sulfur atom is placed

within bonding distance of the center of mass of the top layer of gold atoms of an electrode. In the case of the thiol-terminated alkane, by examining the trajectories we find that it prefers a top–bridge binding as exemplified in Figure 3b. By contrast, the methylthiol-terminated junctions do not have a particular binding geometry.

Importantly, note that the conductance distribution obtained using crushed electrodes and different possible binding configurations coincides with the distribution obtained using the controlled electrode geometry and initial binding ones (top–bridge for C8DT). For C_n SMe the simulations show that the binding configurations do not add additional broadening to the conductance distribution, as the distribution obtained with one trajectory coincides with the one of an ensemble of trajectories with different electrode geometries. For C_n DT, while the binding has a strong influence in the position of the histogram peak, we find that under simulation conditions crushing the electrodes favors top–bridge configurations, and thus the histogram obtained with an ensemble of electrodes is close (albeit slightly broader) to that obtained with a single MD trajectory in a top–bridge configuration.

3.1.3. Role of Thermal Fluctuations. To understand the importance of thermal fluctuations in simulated conductance histograms, we contrasted the conductance distributions generated during a single MD trajectory (Figure 3a, blue lines) with that obtained from an ensemble of trajectories with identical junction configuration but different (and random) initial velocities (Figure 3a, red lines). Furthermore, in the case of C8SMe and C8DT, we also considered an ensemble of

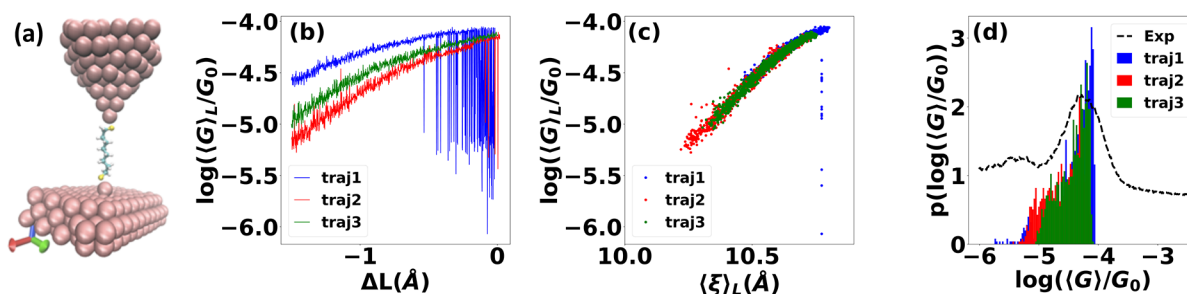


Figure 4. Three time-averaged conductance vs elongation traces for an octane-dithiol (C8DT) junction. (a) Initial geometry of the junction. (b) Time-averaged conductance $\langle G \rangle_L$ vs L . (c) Time-averaged conductance $\langle G \rangle_L$ vs average sulfur-sulfur distance $\langle \xi \rangle_L$. (d) Resulting conductance histograms from each trajectory.

initial conditions with different (precrushed) electrode configurations (Figure 3a, green lines).

As shown in Figure 3a for elongated junctions, the conductance distributions constructed from a single MD trajectory (blue lines) and from an ensemble of trajectories with identical initial gold electrodes (red line) are very similar for all cases considered. Even when an ensemble of different electrode configurations (green line) is considered, the distributions broaden slightly but are very similar to the ones obtained with a single MD trajectory.

These results show that thermal fluctuations captured in a single MD trajectory is the main source for broad distribution of conductance events in elongated junctions. This conclusion applies to conductance distributions generated from all instantaneous snapshots encountered during the dynamics, and it would experimentally correspond to a situation in which the measured conductance reflects instantaneous molecular snapshots.

3.1.4. Comparison with Experiments. The simulated width and shape of the conductance histograms show an (rather excellent) apparent agreement with experimental histograms when the statistics are constructed from either a single MD trajectory, an ensemble of trajectories with identical initial gold electrodes, or different crushed electrodes. The agreement can be observed in Figure 3a for all junction cases— C_n DT and C_n SMe ($n = 4-12$). In the case of C4SMe, we further note that the simulated conductance histogram using an ensemble of trajectories even recovers a conductance shoulder near $\log(G/G_0) = -5.0$ that matches with the experiment. This agreement suggests that it may be possible to mimic experimental histograms using single MD trajectories. However, in spite of this agreement, on physical grounds these simulations are not directly comparable to experiments where currents are averaged over time and cannot resolve individual molecular snapshots.

3.2. Factors Influencing Experimental Conductance Histograms. To better connect with experiments, it is necessary to time-average the conductance $\langle G \rangle_L$ at each point during the elongation L .³⁵ This is because experiments record a time-averaged current, while in the previous section we examined the distribution $p(\log(G/G_0))$ obtained by recording the conductance of all instantaneous molecular snapshots encountered in the dynamics. As discussed below, this additional averaging changes the factors that determine the features of the conductance distribution.

To proceed, we define two length parameters L and ξ . The quantity $L = L_i + vt$ is the elongation of the molecular junction during pulling where L_i is the initial position, v the pulling speed and t time. In turn, ξ is the end-to-end (sulfur-to-sulfur)

molecular length with average $\langle \xi \rangle_L$ at each point L during pulling. The distribution of (time or ensemble) average conductance during pulling is defined as

$$p(\log(\langle G \rangle_L / G_0)) = \frac{1}{|\Delta L|} \int_{L'}^{L_0} p_{L'}(\log(\langle G \rangle_{L'} / G_0)) dL' \quad (2)$$

where $\langle G \rangle_L$ is the (time or ensemble) average conductance at elongation L for a given junction and $p_L(\log(\langle G \rangle_L / G_0))$ the distribution of $\langle G \rangle_L$ in the ensemble of molecular junctions considered. To compute $p(\log(\langle G \rangle_L / G_0))$ we performed simulations in which we determine the average conductance $\langle G \rangle_L$ for each L . These simulations are computationally demanding as they require a different MD simulation for each L during the pulling. Here, averages were obtained by collecting 3.75 ns of MD per L .

3.2.1. Effect of Time-Averaging. Figure 4 shows the time-averaged conductance traces and their distribution for three realizations of the C8DT junction pulling. The three simulations were done using the same initial junction configuration, shown in Figure 4a, and identical pulling conditions. To match the maximum of the experimental conductance histogram (Figure 4d), we chose $E_{Fermi} = -11.4$ eV. As can be seen in Figure 4b, the average conductance $\langle G \rangle_L$ for the three junctions ranges from 10^{-5} to $10^{-4} G_0$, and large conductance fluctuations are observed near junction rupture because of the opening and reforming of molecular junctions. These molecular events were verified by examining the MD trajectories.

In previous sections, we argued that thermal fluctuation in the molecule and electrode determined the conductance distribution. However, once the conductance is averaged over the molecular ensemble accessible at each L , these structural thermal fluctuations determine the value of $\langle G \rangle_L$ but do not play a major role in the observed distribution of time-averaged conductances.

Further, upon time averaging, it is challenging to resolve distinct binding configurations for the alkane-dithiols at a given pulling distance L as the binding configuration can switch between top-top and top-bridge cases. In fact, $\langle G \rangle_L$ captures the average conductance of a molecular ensemble with all possible binding configurations at a given L . Gauche defects or other stable conformers can still influence $\langle G \rangle_L$. In particular, gauche defects are important for small L when the junction is contracted.²⁹ For the range of L considered in Figure 4, these conformers play a minor role.

3.2.2. Stochastic Rupture and the Conductance Dispersion for Identical Molecular Junctions. The current view is that the broad conductance histograms in experiments arises

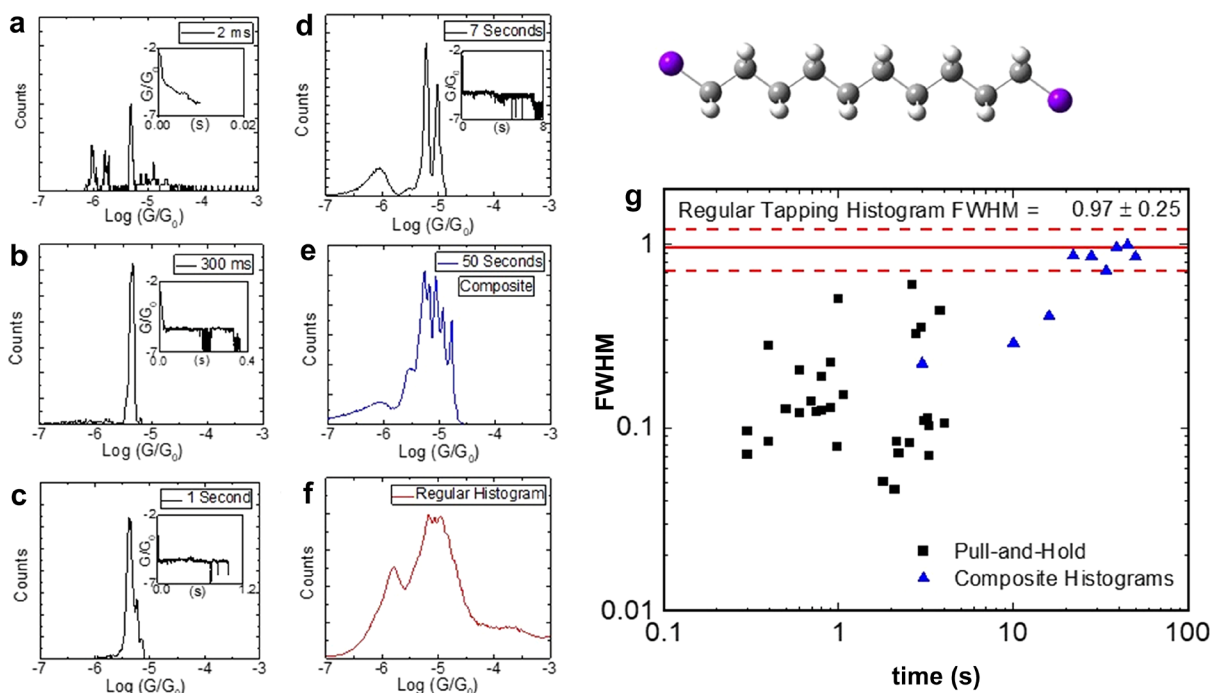


Figure 5. Experimental examination of histogram distributions. (a) Example trace from a single-molecule break junction experiment with a step that lasts 2 ms. (b–d) Histograms of traces obtained using the pull-and-hold method with junctions that last 300 ms (b), 1 s (c), and 7 s (d). Traces are shown in the inset in all cases. (e) Histogram obtained by adding 50 s of traces from pull-and-hold experiments. (f) Example of histogram obtained from normal break-junction process and traces similar to those shown in part a. (g) Plot of fwhm vs step duration for traces obtained by using the pull-and-hold method (black) or by adding several traces into a composite (blue). Once traces are added together, the fwhm becomes similar to that obtained in conventional break-junction histograms (red lines).

because of uncertainties in the junction configuration in and between experiments. However, as clearly shown in Figure 4d, even for single conductance traces with well-defined electrode geometries a broad conductance distribution will still emerge. This is because the conductance can vary over 1 order of magnitude during the last ~ 1 Å of elongation before junction rupture, as can be seen in Figure 4b. This conductance range is close to typical ranges observed in experimental histograms where conductance measurements are done over multiple realizations.

Furthermore, different trajectories with the same initial electrodes and pulling conditions show different $\langle G \rangle_L$ vs L curves (Figure 4b), with different slopes and range of conductance values. This happens when the curves are aligned at rupture points, as is usually done in experiments. However, when plotting the average conductance $\langle G \rangle_L$ against the sulfur–sulfur distance $\langle \xi \rangle_L$ (Figure 4c), the different $\langle G \rangle_L$ vs L curves collapse into a single $\langle G \rangle_L$ vs $\langle \xi \rangle_L$ curve. The specific region, along the $\langle G \rangle_L$ vs $\langle \xi \rangle_L$ curve, where a given $\langle G \rangle_L$ vs L curves fits in depends on the rupture and formation length of the junction in that trajectory. Therefore, the apparent dispersion in the $\langle G \rangle_L$ vs L curves even for identically prepared junctions just reflects the fact that the junction rupture, that determines experimental curve alignment, is a stochastic event.

Usually, a single trajectory (or experimental trace) samples a limited conductance range before the junction breaks. Due to the stochastic nature of the junction rupture, the rupture length is different for every realization. By sampling over several break-junction realizations, ultimately one is sampling over different breaking and formation points for the junction. For this reason, the experimental shape of the histogram is not

recovered with a single trajectory. For this, multiple realizations are necessary that sample over the statistics of junction formation and rupture.³⁵

3.2.3. Break-Junction Experiments. To offer additional experimental insights into these observations, we examined histograms from three types of measurements. The first (Figure 5a) are conventional break-junction experiments where the tip is moving continuously until the junction breaks down, and results in traces ~ 50 ms long. Adding thousands of these together results in the conventional conductance histogram shown in Figure 5f. The second type of measurements are pull-and-hold measurements (Figure 5b–d), where an automated algorithm is used to detect a step in the conductance range of interest and then stop the tip withdrawal until the junction breaks down. These experiments are capable of yielding junctions with lifetimes up to ~ 10 s. The third type of measurement (Figure 5e) adds several of the longer traces together to include times of up to ~ 50 s of junction measurement from multiple junctions.

Individual traces from the first type of experiments result in conductance distributions with several sharp peaks that span 1–2 orders of magnitude in conductance (Figure 5a). As in the computational observations (Figure 4), the changes in conductance during pulling of a single junction can cover a significant range of the values encountered in conventional break-junction histograms.

By contrast, conductance traces obtained from the second type of measurements where the STM is kept fixed at a given distance (Figure 5b–d) results in conductance histograms with a narrower distribution than the one observed in conventional break-junction histograms. This is consistent with the analysis

in Section 3.2.2 as the experiments do not mechanically elongate the junction.

In Figure 5b–d, the observed conductance peaks are broadened because the fluctuations in ξ due to thermal drift of the STM apparatus. Figure S2 in the Supporting Information details the stability of the STM setup and reveals a standard deviation of 0.1 Å in ξ (full width at half-maximum (fwhm) of ~ 0.24 Å). This distance distribution accounts for the observed width of the conductance peaks.

For long enough traces, multiple stable molecular conformations or binding configurations can arise, resulting in a few well-defined peaks as shown in Figure 5d for a 7 s trace. However, to recover the actual shape of the conductance histogram it is necessary to sample over realizations. One trajectory, even very long ones, is not enough to recover the shape. This is also consistent with the simulation analysis and supports the hypothesis that the shape of the conductance histogram is determined by the statistics of junction formation and rupture.

Figure 5g shows the fwhm of the conductance histograms obtained from pull-and-hold traces. As shown, while overall there is an increase in the fwhm with the time a junction is held, a single trace cannot recover the fwhm of conventional break-junction experiments. By combining a few of these long-living traces (Figure 5e) it is possible to recover it (red lines in Figure 5g). This is because each realization is sampling different regions of the $\langle G \rangle_L$ vs $\langle \xi \rangle_L$ curve.

4. CONCLUSIONS

In conclusion, we have examined the factors that determine the width of the conductance histogram in break-junction molecular electronics experiments, in which Au–alkane–Au junctions are involved. Contrary to conventional wisdom, where this width is associated with uncertainties in the electrode shape and junction conformation, we find that even for ideal junctions where such uncertainties do not exist a broad conductance histogram will still emerge. This is because, as seen both in theory and experiment, there is dispersion in conductance that is induced by the process of mechanically elongating the junction that already accounts for the distribution of conductance values encountered in experiments. In turn, the physical factor that determines the shape of the conductance histogram is the stochastic nature of junction rupture and formation. Such stochastic processes are unavoidable in any finite temperature experiment.

Through atomistic simulations, we also studied the conductance distribution in the absence of the inherent time-averaging of currents in experiments. Rather surprisingly, for elongated Au–alkane–Au junctions the geometry of the electrode does not affect this conductance distribution in molecular junctions. Instead, the main source of conductance dispersion comes from thermal fluctuations. In this class of simulations, the conductance distribution obtained from a single MD trajectory essentially coincides with an ensemble of simulations with different electrodes and binding configurations.

From a junction design perspective, to narrow the conductance histogram, as is desirable for the development of single-molecule spectroscopies^{11,13,29,44–51} or molecular devices, it is necessary to identify molecular junctions with a conductance that does not change as they are mechanically strained. This will lead to conductance vs molecular elongation curves that are flat and to a sharp conductance histogram.

From a theory perspective, the key to develop a theory for the conductance histograms (or to develop a microscopic interpretation for existing theories^{52–54}) is to take into account the statistics of junction rupture and formation. These statistics are expected to depend on temperature, pulling speed, the force constant of the STM cantilever, the chemical anchor groups employed, and the details of the electrode.

These results offer detailed atomistic insights into the factors that contribute to the width of the conductance histograms, and they reveal key physical aspects that need to be controlled to narrow their width.

■ ASSOCIATED CONTENT

Supporting Information

The Supporting Information is available free of charge at <https://pubs.acs.org/doi/10.1021/acs.jpcc.0c08428>.

Effect of the Fermi energy in the simulated conductance histograms and stability analysis of the STM setup (PDF)

■ AUTHOR INFORMATION

Corresponding Authors

Joshua Hihath – Department of Electrical and Computer Engineering, University of California Davis, Davis, California 95616, United States; orcid.org/0000-0002-2949-9293; Email: jhihath@ucdavis.edu

Ignacio Franco – Department of Chemistry, University of Rochester, Rochester, New York 14611, United States; Department of Physics, University of Rochester, Rochester, New York 14611, United States; orcid.org/0000-0002-8002-8185; Email: ignacio.franco@rochester.edu

Authors

Zhi Li – Department of Chemistry, University of Rochester, Rochester, New York 14611, United States

Leopoldo Mejía – Department of Chemistry, University of Rochester, Rochester, New York 14611, United States; orcid.org/0000-0003-4534-0191

Jonathan Marrs – Department of Electrical and Computer Engineering, University of California Davis, Davis, California 95616, United States

Hyunhak Jeong – Department of Electrical and Computer Engineering, University of California Davis, Davis, California 95616, United States

Complete contact information is available at: <https://pubs.acs.org/doi/10.1021/acs.jpcc.0c08428>

Notes

The authors declare no competing financial interest.

■ ACKNOWLEDGMENTS

This research is supported in part by the U.S. Office of Naval Research under Award Number N000141612685, and the National Science Foundation under Award Number CBET-1605338 (J.H.) and CHE-1553939 (I.F.).

■ REFERENCES

- (1) Cuevas, J. C.; Scheer, E. *Molecular Electronics: An Introduction to Theory and Experiment*; World Scientific: 2010.
- (2) Ventra, M. D. *Electrical Transport in Nanoscale Systems*; Cambridge University Press: 2008.

- (3) Datta, S. *Electronic Transport in Mesoscopic Systems*; Cambridge University Press: 1997.
- (4) Aviram, A.; Ratner, M. A. *Chem. Phys. Lett.* **1974**, *29*, 277–283.
- (5) Nitzan, A.; Ratner, M. A. *Science* **2003**, *300*, 1384–1389.
- (6) Lindsay, S. M.; Ratner, M. A. *Adv. Mater.* **2007**, *19*, 23–31.
- (7) Reed, M. A.; Zhou, C.; Muller, C. J.; Burgin, T. P.; Tour, J. M. *Science* **1997**, *278*, 252–254.
- (8) Song, H.; Reed, M. A.; Lee, T. *Adv. Mater.* **2011**, *23*, 1583–1608.
- (9) Xu, B.; Tao, N. J. *Science* **2003**, *301*, 1221–1223.
- (10) Hybertsen, M. S.; Venkataraman, L. *Acc. Chem. Res.* **2016**, *49*, 452–460.
- (11) Franco, I.; George, C. B.; Solomon, G. C.; Schatz, G. C.; Ratner, M. A. *J. Am. Chem. Soc.* **2011**, *133*, 2242–2249.
- (12) Wu, C.; Bates, D.; Sangtarash, S.; Ferri, N.; Thomas, A.; Higgins, S. J.; Robertson, C. M.; Nichols, R. J.; Sadeghi, H.; Vezzoli, A. *Nano Lett.* **2020**, *20*, 7980–7986.
- (13) Mejía, L.; Franco, I. *Chem. Sci.* **2019**, *10*, 3249–3256.
- (14) Aradhya, S. V.; Venkataraman, L. *Nat. Nanotechnol.* **2013**, *8*, 399–410.
- (15) Ribas-Arino, J.; Marx, D. *Chem. Rev.* **2012**, *112*, 5412–5487.
- (16) Lörtscher, E.; Weber, H. B.; Riel, H. *Phys. Rev. Lett.* **2007**, *98*, 12–15.
- (17) Engelkes, V. B.; Beebe, J. M.; Frisbie, C. D. *J. Phys. Chem. B* **2005**, *109*, 16801–16810.
- (18) He, J.; Sankey, O.; Lee, M.; Tao, N.; Li, X.; Lindsay, S. *Faraday Discuss.* **2006**, *131*, 145–154.
- (19) Venkataraman, L.; Klare, J. E.; Nuckolls, C.; Hybertsen, M. S.; Steigerwald, M. L. *Nature* **2006**, *442*, 904–907.
- (20) Basch, H.; Cohen, R.; Ratner, M. A. *Nano Lett.* **2005**, *5*, 1668–1675.
- (21) Dhungana, K. B.; Mandal, S.; Pati, R. *J. Phys. Chem. C* **2012**, *116*, 17268–17273.
- (22) Häkkinen, H. *Nat. Chem.* **2012**, *4*, 443–455.
- (23) French, W. R.; Iacovella, C. R.; Rungger, I.; Souza, A. M.; Sanvito, S.; Cummings, P. T. *Nanoscale* **2013**, *5*, 3654.
- (24) French, W. R.; Iacovella, C. R.; Cummings, P. T. *ACS Nano* **2012**, *6*, 2779–2789.
- (25) Li, X.; He, J.; Hihath, J.; Xu, B.; Lindsay, S. M.; Tao, N. *J. Am. Chem. Soc.* **2006**, *128*, 2135–2141.
- (26) Li, C.; Pobelov, I.; Wandlowski, T.; Bagrets, A.; Arnold, A.; Evers, F. *J. Am. Chem. Soc.* **2008**, *130*, 318–326.
- (27) Quek, S. Y.; Venkataraman, L.; Choi, H. J.; Louie, S. G.; Hybertsen, M. S.; Neaton, J. B. *Nano Lett.* **2007**, *7*, 3477–3482.
- (28) Ulrich, J.; Esrail, D.; Pontius, W.; Venkataraman, L.; Millar, D.; Doerrer, L. H. *J. Phys. Chem. B* **2006**, *110*, 2462–2466.
- (29) Mejía, L.; Renaud, N.; Franco, I. *J. Phys. Chem. Lett.* **2018**, *9*, 745–750.
- (30) Paulsson, M.; Krag, C.; Frederiksen, T.; Brandbyge, M. *Nano Lett.* **2009**, *9*, 117–121.
- (31) French, W. R.; Iacovella, C. R.; Rungger, I.; Souza, A. M.; Sanvito, S.; Cummings, P. T. *J. Phys. Chem. Lett.* **2013**, *4*, 887–891.
- (32) Ghane, T.; Kleshchonok, A.; Gutierrez, R.; Cuniberti, G. *J. Phys. Chem. C* **2015**, *119*, 20201–20209.
- (33) Wang, H.; Leng, Y. *J. Phys. Chem. C* **2015**, *119*, 15216–15223.
- (34) Chen, F.; Li, X.; Hihath, J.; Huang, Z.; Tao, N. *J. Am. Chem. Soc.* **2006**, *128*, 15874–15881.
- (35) Li, Z.; Franco, I. *J. Phys. Chem. C* **2019**, *123*, 9693–9701.
- (36) Frisenda, R.; Janssen, V. A. E. C.; Grozema, F. C.; van der Zant, H. S. J.; Renaud, N. *Nat. Chem.* **2016**, *8*, 1099–1104.
- (37) Järvi, T. T.; van Duin, A. C. T.; Nordlund, K.; Goddard, W. A. *J. Phys. Chem. A* **2011**, *115*, 10315–10322.
- (38) Datta, S. *Quantum transport: Atom to transistor*; Cambridge University Press: New York, 2005.
- (39) Renaud, N. *Huskython: Quantum Transport for Molecular Junctions in Python*; 2018; <https://github.com/NicoRenaud/huskython>.
- (40) Hutchesson, J.; Franco, I.; Renaud, N.; Carignano, M.; Ratner, M. A.; Schatz, G. C. *TRANSPull: Computes Pulling Coupled to Transport Properties of Single Molecules*; 2011; <https://nanohub.org/resources/11739>.
- (41) Park, Y. S.; Whalley, A. C.; Kamenetska, M.; Steigerwald, M. L.; Hybertsen, M. S.; Nuckolls, C.; Venkataraman, L. *J. Am. Chem. Soc.* **2007**, *129*, 15768–15769.
- (42) Frei, M.; Aradhya, S. V.; Hybertsen, M. S.; Venkataraman, L. *J. Am. Chem. Soc.* **2012**, *134*, 4003–4006.
- (43) Aradhya, S. V.; Nielsen, A.; Hybertsen, M. S.; Venkataraman, L. *ACS Nano* **2014**, *8*, 7522–7530.
- (44) Li, Z.; Tkatchenko, A.; Franco, I. *J. Phys. Chem. Lett.* **2018**, *9*, 1140–1145.
- (45) Koch, M.; Li, Z.; Nacci, C.; Kumagai, T.; Franco, I.; Grill, L. *Phys. Rev. Lett.* **2018**, *121*, 047701.
- (46) Franco, I.; Schatz, G. C.; Ratner, M. A. *J. Chem. Phys.* **2009**, *131*, 124902.
- (47) Pirrotta, A.; De Vico, L.; Solomon, G. C.; Franco, I. *J. Chem. Phys.* **2017**, *146*, 092329.
- (48) Pirrotta, A.; Solomon, G. C.; Franco, I. *J. Phys. Chem. C* **2016**, *120*, 19470–19478.
- (49) Pirrotta, A.; Solomon, G. C.; Franco, I.; Troisi, A. *J. Phys. Chem. Lett.* **2017**, *8*, 4326–4332.
- (50) Li, Y.; Artés, J. M.; Demir, B.; Gokce, S.; Mohammad, H. M.; Alangari, M.; Anantram, M.; Oren, E. E.; Hihath, J. *Nat. Nanotechnol.* **2018**, *13*, 1167–1173.
- (51) Ramachandran, R.; Li, H. B.; Lo, W.-Y.; Neshchadin, A.; Yu, L.; Hihath, J. *Nano Lett.* **2018**, *18*, 6638–6644.
- (52) Quan, R.; Pitler, C. S.; Ratner, M. A.; Reuter, M. G. *ACS Nano* **2015**, *9*, 7704–7713.
- (53) Reuter, M. G.; Hersam, M. C.; Seideman, T.; Ratner, M. A. *Nano Lett.* **2012**, *12*, 2243–2248.
- (54) Williams, P. D.; Reuter, M. G. *J. Phys. Chem. C* **2013**, *117*, 5937–5942.